

Constituent properties of HMX needed for mesoscale simulations

Ralph Menikoff and Thomas D Sewell

Theoretical Division, Los Alamos National Laboratory, Los Alamos, NM 87545, USA

Received 9 April 2001, in final form 10 January 2002

Published 20 February 2002

Online at stacks.iop.org/CTM/6/103

Abstract

Plastic-bonded explosives are heterogeneous materials. Improved burn models for weak initiation relevant to accident scenarios require a better understanding of the physics associated with the formation and growth of hot spots. Since the relevant length scale is subgrain in extent, mesoscale simulations are needed to study hot spots. Mesoscale simulations require as input constitutive properties of an explosive grain. In addition, it is essential to account for physical dissipative mechanisms since hot spots represent local peaks in the fluctuations of the temperature field. Here, constitutive properties of the explosive HMX needed for mesoscale simulations are discussed and experimental data reviewed. Because some decomposition may occur during a measurement, it is difficult to account for systematic error in the data. To get a sense of the uncertainties in material parameters, it is necessary to examine all the available data. In addition, we discuss results from molecular dynamics simulations of some properties for which experimental data are lacking.

1. Introduction

Hot spots dominate initiation of heterogeneous explosives, such as plastic-bonded explosives (PBXs). This has been widely recognized since the 1950s [1]. Early simulations of hot-spot initiation (see e.g. [2] and references therein) were limited by the computational resources available at the time. With the recent great advances in computer power, in terms of both speed and memory size, there is a renewed interest in understanding initiation based on simulations in which hot spots are fully resolved; see e.g. [3–5]. These are referred to as ‘mesoscale’ simulations, and are motivated, in part, by the need to predict thresholds for weak initiation in accident scenarios and the effects of ageing on explosive performance. In addition, hot spots affect explosive properties such as shock desensitization, failure diameter and the ability of a detonation wave to turn corners.

Simulations at the mesoscale require constitutive properties that incorporate more detailed physics than used for engineering applications. Fine resolution engineering-scale simulations typically use a cell size of 1 mm. This is ten times the average size of a grain in an explosive such as PBX-9501. Consequently, engineering simulations can make use of average properties. For

example, though an individual grain is a crystal, and hence anisotropic [6], coarse grain average properties are isotropic due to the presumed randomness of the crystal orientation. Moreover, when hot spots are not resolved, their effect on the average reaction rate is accounted for with empirical burn models. Typically, for numerical stability, these burn models are based more on pressure than on temperature. In contrast, simulations of hot-spot initiation should use the chemical reaction rate of the explosive. Since the reaction rate is highly sensitive to temperature, thermal properties are critical for mesoscale simulations. Furthermore, hot spots represent highly localized spatial fluctuations in the temperature field. These fluctuations depend on both material inhomogeneities and dissipative mechanisms.

Here, we restrict our attention to the explosive HMX (cyclo-tetramethylene-tetranitramine, $\text{C}_4\text{H}_8\text{N}_8\text{O}_8$). In addition to use in high-performance PBXs, HMX is used as a component of propellants. We focus on the thermodynamic region relevant to weak initiation, i.e. temperature up to 1000 K and pressure up to 3 GPa. Key constitutive properties are discussed and the available data reviewed. Unlike inert materials, key parameters of HMX are difficult to measure above melting due to the onset of rapid chemical reaction. Molecular dynamics simulations provide a means to supplement experimental data for some of the needed material properties and to provide estimates of parameters where data are completely lacking [7–14]. The following sections cover crystallographic, thermal, mechanical and transport properties. The reaction rate of HMX and microstructure of a PBX are being studied by others and are not covered here; see e.g. [15–17].

2. Crystallography

Four solid phases of HMX have been produced and identified at ambient conditions [18]. These are denoted as α , β , γ and δ . The crystal structure of each phase has been determined by x-ray and/or neutron diffraction [19–22]. For ignition the β and δ phases are important. The other two phases are neglected since the α -phase has a limited domain of stability while the γ -phase is actually an H_2O –HMX complex. In addition, there is evidence for two other high-pressure phases; see [23].

The β -phase has the highest density and is most stable under ambient conditions. The crystal structure of β -HMX is monoclinic¹. As the temperature is raised, the δ -phase becomes thermodynamically stable. The δ -phase has a hexagonal crystal structure. As discussed later, the crystal structure also serves in other experiments as a means to determine crystal density.

At atmospheric pressure, a transition to the δ -phase begins around 438 K (165°C). The transition dynamics is governed by Arrhenius kinetics [25, 26]. As a consequence, below the transition temperature the δ -phase is a long-lived metastable polymorph. At the melting temperature, 552 K (279°C), the β – δ transition rate extrapolates to $\sim 40 \text{ s}^{-1}$. As a result, measured transition temperatures depend on heating rates; see e.g. [27, table 3]. Moreover, Henson and co-workers [28, 15] have fit the time-dependent concentration of the δ -phase during the transition with a nucleation and growth model. Nucleation is sensitive to impurities. Some synthesis processes for HMX result in RDX impurities on the per cent level. A further complication is that some decomposition occurs during the transition [29, 30]. Both impurities and decomposition affect measurements of the transition temperature. Finally, above 521 K (248°C) the δ -phase is more stable than the β -phase at any pressure [30].

¹ A point of confusion is that the lattice parameters can be specified in either of two equivalent space groups: $\text{P2}_1/\text{n}$ or $\text{P2}_1/\text{c}$. Both unit cells have two molecules with lattice vectors $a = 6.54 \text{ \AA}$ and $b = 11.05 \text{ \AA}$ and lattice angles $\alpha = \gamma = 90^\circ$. One molecule is at a lattice point. For $\text{P2}_1/\text{n}$ the second molecule is cell centred, and the other lattice parameters are $c = 7.37 \text{ \AA}$, $\beta = 102.8^\circ$ [24]. Alternatively, for $\text{P2}_1/\text{c}$ the second molecule is centred on the b – c face, and the other lattice parameters are $c = 8.70 \text{ \AA}$ and $\beta = 124.3^\circ$ [20]. From here on, the $\text{P2}_1/\text{n}$ space group is used.

Under the slow heating of a cook-off experiment, the β - δ transition is important for thermal ignition. Henson and co-workers [31] proposed that the β - δ transition is the first step of HMX decomposition. The change in enthalpy is 33.2 kJ kg^{-1} and the volume expansion $((V_\delta - V_\beta)/V_\beta)$ is 8%. The enthalpy change corresponds to a temperature change of $\sim 200 \text{ K}$, which is large enough to have a significant effect on the reaction rate. When HMX is confined, instead of a volume increase the pressure increases by $\sim 1 \text{ GPa}$. This in turn would increase the transition temperature from the ambient value of 438 K to the limiting value of 521 K .

In addition to the change in crystal symmetry, the molecular conformation changes in the transition from chair-like to boat-like. The chair-like conformation has an inversion centre while the boat-like does not. As a consequence, the HMX molecule in the δ -phase has a dipole moment and the δ -phase is an excellent second harmonic generator [26]. The change in the second harmonic generation provides a diagnostic technique for measuring the progress of the β - δ transition.

The δ -phase can also be produced when an explosive is damaged [16,32]. This is important for accident scenarios because the δ -phase, while only metastable at ambient conditions, is long-lived with a higher reaction rate and hence more sensitive to ignition than the β -phase [27, table 6]. The difference in reaction rates is not understood, but is very likely related to the conformation change and/or volume change between the β -phase and the δ -phase.

Fast heating during shock loading, in contrast, may lead to a direct transition from the β -phase to the liquid phase. In this case, the melting transition is likely the first step of HMX decomposition. Melting is discussed in more detail in the following section.

The thermal expansion of all four HMX polymorphs has been measured using x-ray diffraction [27,24], and calculated using molecular dynamics [9, 14]. Expansion is highly anisotropic. For β -HMX the linear expansion coefficients are $(-0.29, 12, 2.3) \times 10^{-5} \text{ K}^{-1}$ along the (a,b,c) axes. We note that the sign of the expansion coefficient is negative along the a -axis. In addition, $d \ln(\beta)/dT = 2.6 \times 10^{-5} \text{ K}^{-1}$. Within a PBX, the large anisotropy would undoubtedly give rise to cracking and debonding of HMX grains under thermal stresses. Such added heterogeneities would enhance the formation of hot spots and thus increase ignition sensitivity.

3. Thermal properties

3.1. Melt curve

Plastic work and shear heating are among the dissipative mechanisms leading to hot-spot formation. Upon melting, the yield strength vanishes and the shear viscosity decreases by orders of magnitude. Consequently, melting limits the peak hot-spot temperature achievable from these two dissipative mechanisms to the melt temperature. Since reaction rates are extremely sensitive to temperature, an important quantity for initiation due to a weak compressive load is the melt temperature as a function of pressure.

The Kraut–Kennedy relation is a linearization of the melt curve

$$T_m = T_{m0} \left(1 + a \frac{\Delta V}{V_0} \right). \quad (1)$$

Based on the Lindemann law (see [33, section 5.3.2]), the constant can be estimated as $a = 2(\Gamma - \frac{1}{3})$. For HMX the Grüneisen coefficient is $\Gamma = 1.1$ at ambient conditions [34], yielding $a = 1.53$.

Table 1. HMX parameters² needed for estimate of slope of melt curve.

$L_{\delta \rightarrow \text{liq}}$	0.202	MJ kg^{-1}	Estimate ^a
Γ	1.1	—	Inferred from thermodynamics ^b [34]
C_P	1.65×10^{-3}	$\text{MJ kg}^{-1} \text{K}^{-1}$	Extrapolated to $T = 550 \text{ K}$ [36]
ρ_δ	1.71	g cm^{-3}	Extrapolated to $T = 550 \text{ K}$ [24]
ρ_{liq}	1.65	g cm^{-3}	At $T = 550 \text{ K}$ [7]
K_T	15.8	GPa	For δ -phase, estimate ^c

^a Estimate based on $L_{\delta \rightarrow \text{liq}} = L_{\beta \rightarrow \text{liq}} - L_{\beta \rightarrow \delta}$ and the values in [37] of $L_{\beta \rightarrow \delta} = 9.832 \text{ kJ mol}^{-1}$ and $L_{\beta \rightarrow \text{liq}} = 69.873 \text{ kJ mol}^{-1}$.

^b $\Gamma = \beta K_T V / (C_P - \beta^2 K_T T V)$ where β is the coefficient of volumetric expansion. The values of β , K_T and C_P have been measured experimentally.

^c For β -HMX, the experimental value of K_T is 13.5 GPa [34]. Molecular dynamics simulations [9, 14] give $K_T = 10.2$ and 11.9 for the β - and δ -phase, respectively. The estimate of K_T for δ -HMX is based on multiplying the value from the molecular dynamics simulation by the ratio of the experimental to simulated values of β -HMX.

Alternatively, the parameter a can be determined from thermodynamics. The Clausius–Clapeyron relation and standard thermodynamic identities yield

$$\begin{aligned} \left. \frac{dP}{dT} \right|_{\text{coex}} &= \frac{\Delta S}{\Delta V} = \frac{L}{T \Delta V} \\ &= \frac{\Gamma}{V} C_V - \left[\rho K_S - \left(\frac{\Gamma}{V} \right)^2 C_V T \right] \left. \frac{dV}{dT} \right|_{\text{coex}}, \end{aligned}$$

where the phase transition is characterized by the latent heat L , entropy difference between the phases $\Delta S = L/T$ and the change in specific volume ΔV . Here, K_S is the isentropic bulk modulus and C_V is the specific heat. Upon substituting $dT/dV|_{\text{coex}} = -a T_{m0}/V_0$, the equation can be rearranged to yield

$$a = \frac{V K_S - \Gamma^2 C_V T}{L - (\Delta V/V) \Gamma C_V T} \frac{\Delta V}{V}. \quad (2)$$

Since thermodynamic relations hold only in equilibrium, the appropriate coexistence curve is between the δ -phase and the liquid.

From experimental data and molecular dynamics simulations, the relevant parameters are listed in table 1. Substituting these values in (2) gives $a = 1.79$. Considering all the uncertainties in the value of the thermodynamic quantities, this is compatible with the estimate of a based on the Lindemann law. In the following, the average value $a = 1.66$ is used.

Numerical simulations frequently linearize the melt curve as a function of pressure:

$$T_m = T_{m0} + bP. \quad (3)$$

The coefficients a and b are related by $b = a T_{m0}/K_T$. This gives $b = 58 \text{ K GPa}^{-1}$. In the literature, a value as high as $b = 180 \text{ K GPa}^{-1}$ has been used [35, equation (9) and table III]. Extrapolation of the melt temperature based on V or P makes a considerable difference. Figure 1 shows the temperature behind a shock as a function of pressure and also the melt temperature based on equations (1) and (3). With (1), T_m approaches an asymptotic value since the shock compression ratio has a maximum value on the Hugoniot locus. For this model of HMX, melting would occur for shock pressures above 19 GPa. In contrast, with 3 the melt temperature rises faster than the shock temperature and HMX would not melt under shock loading.

² Values of parameters are given in a consistent set of units corresponding to length in mm, time in μs and mass in mg.

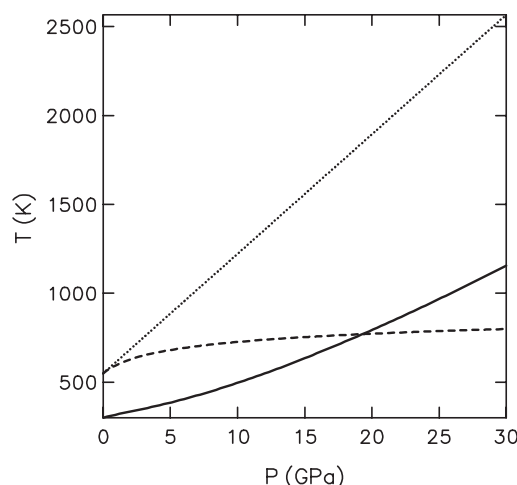


Figure 1. Temperature as a function of pressure on shock Hugoniot. The solid curve is the shock temperature based on Hayes EOS. The dashed curve is the melt temperature based on equation (1) with $a = 1.65$. The dotted line is the melt temperature based on the corresponding linearization in pressure.

The melt curve is difficult to measure for an explosive. Typically, the time constant for a thermal explosion becomes very small upon melting. For HMX, sugar is used as an inert mock-up [38]. Both are large organic molecules, form monoclinic crystals³ and have a similar mechanical response. Due to the importance of the melt curve, it would be worthwhile to measure the melt curve for sugar in order to assess the validity of the extrapolations in V and P .

Another important effect of melting is related to the vapour pressure. The vapour pressure of solid HMX is extremely low. However, the vapour pressure is roughly exponential in the inverse temperature; see [41, figure 2] and references therein. The boiling point at atmospheric pressure is estimated to be 771 K. At this temperature, the adiabatic induction time is of the order of $10 \mu\text{s}$. Simple models for deflagration waves in HMX [42] include a melt layer followed by pyrolysis and gas combustion with a gap between the flame front and the liquid interface (stand-off distance). This is accurate in the low-pressure regime of propellant applications. However, even weak initiation occurs at pressures greater than a kilobar, and such pressures will suppress the vaporization and very likely have a large effect on the decomposition mechanism.

3.2. Specific heat

The temperature can be expressed as

$$T(V, e) = \underbrace{T_0 \left(\frac{V_0}{V} \right)^\Gamma}_{\text{isentropic compression}} + \underbrace{\frac{e - e_s(V)}{C_V}}_{\text{dissipative heating}},$$

where the subscript s denotes a value on the initial isentrope and C_V is the specific heat at constant volume. For pressures up to 10 GPa (which limits the compression ratio to

³ Table sugar or sucrose, $\text{C}_{12}\text{H}_{22}\text{O}_{11}$, forms monoclinic crystals with space group $\text{P}2_1$. The lattice parameters are $a = 10.86 \text{ \AA}$, $b = 8.71 \text{ \AA}$, $c = 7.76 \text{ \AA}$ and $\beta = 102.95^\circ$ [39, 40]. The molecular weight is 342 and the density is 1.58 g cm^{-3} . See footnote 1 for lattice parameters of β -HMX ($\text{C}_4\text{H}_8\text{N}_8\text{O}_8$, $\text{P}2_1/\text{n}$, molecular weight 296, density 1.9 g cm^{-3}).

$V_0/V < 1.3$) and $\Gamma = 1.1$, the temperature increase from isentropic compression is less than 100 K. Reaction on a fast time scale ($\lesssim 10 \mu\text{s}$) requires a temperature of at least 700 K. Therefore, the temperature increase must be at least 400 K, and the bulk of the temperature rise must come from dissipative heating which is inversely proportional to C_V . Consequently, the specific heat is a critical parameter for the determining the hot-spot temperature.

The specific heat at constant pressure, C_P , has been measured for β -HMX and δ -HMX [36, 43, 44]. The specific heat as a function of temperature is nearly the same for both phases. At atmospheric pressure, C_P for β -HMX varies nearly linearly from $1.0 \times 10^{-3} \text{ MJ kg}^{-1} \text{ K}^{-1}$ at room temperature (294 K) to $1.4 \times 10^{-3} \text{ MJ kg}^{-1} \text{ K}^{-1}$ at the δ -phase transition (438 K). Above the phase transition, the measurements differ substantially. Very likely some decomposition occurs and the results are sensitive to the experimental setup. There are no data for specific heat in the liquid phase. Molecular dynamics simulations are likely to be the only means of obtaining specific heats in the liquid regime.

The specific heat at constant V can be determined from the thermodynamic relation

$$C_V = C_P - \beta^2 T V K_T.$$

Substituting the measured values for the volumetric thermal expansion $\beta = 1.31 \times 10^{-4} \text{ K}^{-1}$, and the isothermal bulk modulus $K_{T0} = 13.5 \text{ GPa}$, one finds that $(C_P - C_V)/C_P$ is 5.4% at room temperature.

The specific heat is dominated by the excitations of the vibrational modes of HMX molecules. The vibrational spectrum of β -HMX has been determined using quantum chemistry calculations [41, table 2]. In addition, Goddard and co-workers⁴ have calculated the spectrum and then used it in conjunction with molecular dynamics simulations to determine the temperature dependence of C_V in the range $0 < T < 3000 \text{ K}$. The specific heat is a monotonically increasing function of temperature: 0.8 at 300 K, 1.2 at 500 K, 1.7 at 1000 K, 1.9 at 1500 K, in units of $\text{J g}^{-1} \text{ K}^{-1}$. By 3000 K the specific heat is levelling off at $2.1 \times 10^{-3} \text{ MJ kg}^{-1} \text{ K}^{-1}$, which corresponds to $(3 \times 28 - 8)R/W = 2.14 \times 10^{-3} \text{ MJ kg}^{-1} \text{ K}^{-1}$, where R is the universal gas constant $8.317 \text{ J K}^{-1} \text{ mol}^{-1}$ and W is the molecular weight ($0.296 \text{ kg mol}^{-1}$). This is the expected value based on a contribution to the specific heat of R/W per vibrational degree of freedom (3×28 atoms per molecule) less the eight vibrational degrees of freedom corresponding to the C–H bond stretching. The vibrational frequencies of the C–H bonds are very high and consequently those modes are not highly populated. Based on the measured value at room temperature, the accuracy of the calculated specific heat is probably 10–20%.

Typically, equations of state used for HMX in numerical simulations treat C_V as constant with a value corresponding to that at the melt temperature (552 K), $1.5 \times 10^{-3} \text{ MJ kg}^{-1} \text{ K}^{-1}$. At 1000 K the specific heat has increased by an additional 40%. Thus, in the regime of interest for hot-spot initiation, the approximation of a constant C_V introduces a large error in the hot-spot temperature. This in turn will affect the reaction rate by orders of magnitude. Consequently, for quantitatively accurate simulations of hot-spot initiation, good thermal models as well as mechanical models for the explosive are needed.

4. Mechanical properties

The stress tensor⁵ is usually split into a hydrostatic component and a deviatoric component:

$$\sigma = P\mathbb{I} + \sigma', \quad (4)$$

⁴ Private communications, Professor W A Goddard III Cal. Tech., 2001.

⁵ We use the convention in which stress is positive in compression and negative in tension. Likewise, strain is positive in compression and negative in expansion.

where $P = \frac{1}{3} \text{Tr } \sigma$ is the pressure. The deviatoric stress is associated with the strength model for a solid. It vanishes for the liquid phase and for gaseous reaction products. The magnitude of the stress deviator is limited by the yield stress. Consequently, the pressure is the dominant term at high stress.

4.1. Hydrostatic stress

Hydrostatic compression of HMX is achieved by suspending small crystals in a fluid and then placing the sample in either a Bridgman anvil [34] or a diamond anvil [23]. The density of the crystals is determined via x-ray diffraction measurements of the lattice parameters. The pressure is deduced either from the compression of an NaF crystal added to the mixture or from ruby fluorescence. For a comparison of these two data sets, see [45].

At high pressures, an alternative method may be used. Samples of HMX are solvent pressed to achieve a low porosity (about 0.5%). Due to the random orientation of the crystals, on a coarse grain scale the sample response is homogeneous. Standard Hugoniot measurements are then performed [46, p 596]. In addition, three high-pressure Hugoniot points have been obtained from wedge shots on single-crystal HMX [47]. Though shock compression is uniaxial, above the yield stress the pressure dominates the stress deviator⁶. All the available data for HMX, isothermal and shock Hugoniot, are shown in figure 2.

Of particular importance is the bulk modulus,

$$K_T = -V \left. \frac{dP}{dV} \right|_T,$$

and its pressure derivative K'_T , at the initial state. The isothermal data are not sufficiently precise to obtain derivatives by finite differences. Instead, fitting forms are used as a means of smoothing the data. Olinger *et al* [34] used the Hugoniot relations

$$\begin{aligned} \frac{V}{V_0} &= 1 - \frac{u_p}{u_s}, \\ P &= P_0 + \rho_0 u_p u_s \end{aligned}$$

to transform to pseudo-particle velocity u_p and pseudo-shock velocity u_s variables. In the (u_p, u_s) -plane, their data are well fit by a straight line, $u_s = c_T + s_T u_p$ where c_T is the bulk isothermal sound speed. This yields $K_T = 13.5$ GPa and $s_T = (K'_T + 1)/4 = 2.6$. The fit is shown as the black lines in figure 2.

Using thermodynamic relations, the isentropic bulk modulus can be obtained from the isothermal modulus:

$$K_S = K_T + \Gamma \rho C_V T. \quad (5)$$

The values of the isentropic bulk modulus and sound speed are then $K_S = 14.3$ GPa and $c_s = 2.74$ mm μs^{-1} . Also, assuming that K_T is a function of density only (i.e. the temperature dependence of K_T is dominated by the density change due to thermal expansion), the derivatives of the bulk moduli are related by

$$K'_T = K'_S + \frac{\Gamma^2 C_V T}{V K_T} (K'_S + 1 - \Gamma). \quad (6)$$

Thus, the isothermal data can be used to obtain isentropic parameters. The isentropic values, K_S and K'_S , determine a linear u_s - u_p relation for the principal Hugoniot locus.

⁶ In addition, for the solvent-pressed samples, porosity increases the compression ratio behind a shock and increases the shock heating. Consequently, for fixed particle velocity, porosity lowers the shock velocity. The porosity has a slight effect when comparing with single-crystal data.

This leads to a Mie–Grüneisen equation of state for HMX of the form

$$P(V, e) = P_h(V) + \frac{\Gamma}{V} (e - e_h(V)),$$

where the principal Hugoniot locus is used as the reference curve:

$$P_h(V) = \frac{V_0 - V}{[V_0 - s(V_0 - V)]^2} c^2,$$

$$e_h(V) = \frac{1}{2} P_h(V) \cdot (V_0 - V).$$

Olinger *et al* derived $c = 2.74 \text{ mm } \mu\text{s}^{-1}$ and $s = 2.6$ from their data. Based on the thermodynamic identity

$$\frac{\Gamma}{V} = \frac{\beta K_S}{C_P}, \quad (7)$$

and the measured values of density $V^{-1} = 1.9 \text{ g cm}^{-3}$, specific heat $C_P = 1.05 \times 10^{-3} \text{ MJ kg}^{-1} \text{ K}^{-1}$ and coefficient of volumetric expansion $\beta = 1.47 \times 10^{-4} \text{ K}^{-1}$, they deduced $\Gamma = 1.1$. The HMX equation of state derived by Olinger *et al* is frequently used in numerical simulations.

Yoo and Cynn [23] fit their data to a third-order Birch–Murnaghan equation of state (see e.g. [33, p 64])

$$P(V) = \frac{3}{2} K_{T0} \left[\left(\frac{V_0}{V} \right)^{7/3} - \left(\frac{V_0}{V} \right)^{5/3} \right] \left[1 + \frac{3}{4} (K'_{T0} - 4) \left[\left(\frac{V_0}{V} \right)^{2/3} - 1 \right] \right]. \quad (8)$$

The fit is shown as the red lines in figure 2. Clearly, the HMX equation of state based on the data of Yoo and Cynn is much softer than that based on the data of Olinger *et al*.

The difference in the equation of state is particularly significant when the fit of Olinger *et al* is extrapolated to CJ conditions: $P \approx 40 \text{ GPa}$ and $u_s \approx 9 \text{ mm } \mu\text{s}^{-1}$. For mesoscale simulations of initiation, the shock temperature is critically important due to the strong temperature dependence of the reaction rate. The temperature behind a strong shock is approximately $u_p^2/2C_V$. At the CJ-detonation velocity, the shock temperature would be several hundred degrees hotter based on the Birch–Murnaghan fit to the data of Yoo and Cynn than on the linear u_s-u_p fit to the data of Olinger *et al*. Such a temperature difference would change the reaction rate by several orders of magnitude.

The discrepancy in the fits is due in part to the assumption of a linear u_s-u_p relation. The linear relation is well documented for metals. However, in contrast to atomic metals, explosives are typically large organic molecules. The compression curve for a molecular crystal has a distinctively different behaviour than that of an atomic crystal. Namely, at pressures up to a few tenths of GPa, the bulk modulus increases rapidly with compression. This shows up as a curvature in the graph of $u_s(u_p)$ for small u_p . Data for PETN (penta-erythritol-tetranitrate, $\text{C}_5\text{H}_8\text{N}_4$) illustrates the curvature effect very clearly [48]. For the parameters that fit the data of Yoo and Cynn, the Birch–Murnaghan form of equation of state displays a significant curvature effect. The curvature at low u_p affects the slope of the fit at higher u_p , and is a major cause of the large discrepancy when the two forms of equations of state are extrapolated to CJ-detonation velocity. In addition, there are systematic differences between the data sets due to differences in experimental technique; see [45] for a more detailed discussion.

The first data point of both Olinger *et al* and Yoo and Cynn is above 1 GPa. Since isothermal data are not available in the low-pressure regime in which the curvature of $u_s(u_p)$ is large, we look for consistency with the available Hugoniot data. Both isothermal and Hugoniot data are shown in figure 2. Below 10 GPa, the HMX Hugoniot data are based on solvent-pressed samples [46, p 596]. In this regime the thermal pressure due to shock heating is small relative

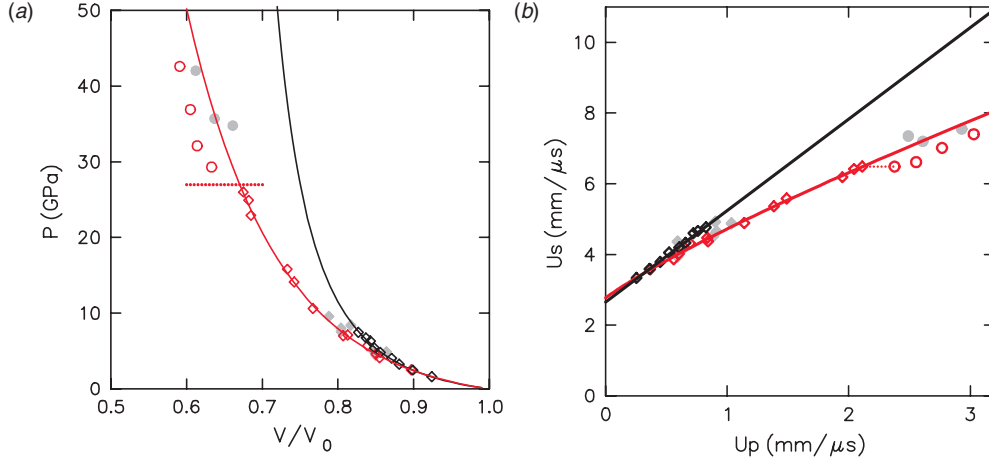


Figure 2. HMX compression data: Black symbols are isothermal data from [34] and black lines correspond to the linear u_s-u_p fit. Red symbols are isothermal data from [23] and red lines correspond to the Birch-Murnaghan fit. Grey symbols are Hugoniot data: diamonds are for solvent-pressed samples [46, p 596] and circles are single-crystal data [47]. The dotted red line indicates the high-pressure phase. Red circles are data points above the phase transition and not used in the fits.

to the pressure from shock compression. Consequently, the isothermal and Hugoniot data are quite close to each other.

Three high-pressure Hugoniot points are based on single-crystal (unspecified orientation) wedge experiments of Craig [47] (also listed in [46, p 595]). These are also plotted in figure 2. For strong shocks the Hugoniot data should lie above the isothermal data due to shock heating. Prior to Yoo and Cynn's recent experiment, Dick [49] and Bernecker [50] suggested a high pressure shock-induced phase transition in HMX based on the fact that the high-pressure Hugoniot data lay considerably below the linear fit to the data of Olinger *et al.* This led Bernecker [50] to propose approximating the Hugoniot locus with a piecewise linear fit. The Birch-Murnaghan fit to Yoo and Cynn's data is effectively a smooth version of Bernecker's fit that interpolates between the low-pressure data of Olinger *et al.* (except for their three highest-pressure data points) and the higher-pressure data of Yoo and Cynn. Consequently, on the basis of the fit to Yoo and Cynn's data, a shock-induced phase transition would not be warranted.

Since the Birch-Murnaghan fit is compatible with both isothermal and Hugoniot data for HMX, it is natural to use it to construct an equation of state. For this purpose, an equation of state may be constructed based on the functional form of Helmholtz free energy used by Hayes [51, appendix B]. Incorporating a Debye model term in the free energy to account for lattice vibrations would allow the measured temperature variation of the specific heat to be approximated. Another advantage of a complete equation of state based on the free energy is that phase transitions can be accounted for in a thermodynamically consistent manner by combining two such forms [51, 52]: e.g. one for solid HMX and a second for liquid HMX. This could be used to predict the melt curve. One difficulty is that there are presently no $P-V$ data for the liquid phase. Since the reaction rate of HMX increases very rapidly upon melting, it is very difficult to make measurements on the liquid phase. However, molecular dynamics simulations should be able to determine accurately the liquid isotherm.

Craig's [47] single-crystal experiments are particularly noteworthy. A shock of 34 GPa failed to transit to a detonation wave within the 7.4 mm length of the HMX sample. We note

that the Chapman–Jouget pressure for PBX-9404 (94% HMX by weight) is 36 GPa. This indicates that a single crystal is very insensitive. Moreover, since the length of run is much greater than the reaction zone width [2, table 1.4, p 23] for a detonation wave in PBX-9404, hot spots evidently play a role in propagating a detonation wave.

At 34 GPa the computed temperature is approximately 1300 K. This may vary by ± 200 K depending on estimates for specific heat and the density dependence of the bulk modulus. Craig’s experiment places a lower bound of $1 \mu\text{s}$ on the induction time. This is much longer than the induction time computed from Arrhenius parameters based on calorimeter experiments for the liquid phase [53], and implies that the single-crystal reaction rate is much lower than that typically used for HMX [2, p 218]. The reaction rate may depend on the polymorphic form or on pressure in addition to temperature, as indicated by the calorimeter experiments of Lee *et al* [54].

Finally, we note that the hydrostatic experiments give more information than just $P(V)$ along an isotherm. They also determine the pressure dependence of the lattice parameters. From the lattice parameters, the full strain tensor, corresponding to a hydrostatic stress $\sigma = P\mathbb{I}$, can be computed as follows. Let \mathbf{h} be the transformation matrix from the crystal to Cartesian coordinates. Then the strain tensor is given by

$$\epsilon(P) = \frac{1}{2} ([\mathbf{h}(P)\mathbf{h}^{-1}(P_0)]^T [\mathbf{h}(P)\mathbf{h}^{-1}(P_0)] - \mathbb{I}),$$

where the subscript 0 denotes the reference state at which the strain vanishes. We note that this formula is used in molecular dynamics calculations of the elastic coefficients based on fluctuations in the strain tensor; see e.g. [9, 13].

For the isothermal experiments, the anisotropic response of a crystal results in the strain tensor having non-hydrostatic components even though the stress tensor is hydrostatic. A measure of the shear strain is given by $\|\epsilon - \frac{1}{3}(\text{Tr } \epsilon)\mathbb{I}\|/\|\text{Tr } \epsilon\|$. From the experimental data, the shear strain is about 20% of the volumetric strain. This helps to explain the observation of Yoo and Cynn [23], based on the Raman spectrum, of a phase transition with negligible volume change at 12 GPa. They suggested that the phase transition is martensitic. Martensitic phase transitions are usually induced by shear strain. This is compatible with the shear strain inferred from the lattice parameters.

4.2. Yield strength

Single-crystal wave profiles give information on material strength. Dick and co-workers [55, 56] performed a series of gas gun experiments in which an HMX crystal is shock loaded to 1.4 GPa; a projectile from a gas gun impacts an x -cut quartz front disc and transmits shock into the HMX crystal. VISAR⁷ data for velocity at the back of the sample (HMX/PMMA interface) for two crystal orientations and three sample lengths [58, 56] are shown in figure 3. The important qualitative features of the wave profiles are:

- A split wave is clearly displayed. It is composed of an elastic precursor followed by a plastic wave. The rise time of the elastic precursor is very abrupt while the rise time of the plastic wave is ~ 100 ns.
- The amplitude of the precursor decays with length of run to a non-zero asymptotic value.
- At 3 mm length of run (middle curves in figure 3), the response between the precursor and plastic wave depends on the orientation.

These are the classic wave properties associated with an elastic–plastic crystal. In particular, the plastic response is rate dependent and anisotropic.

⁷ Velocity Interferometry System for Any Reflector; for a review of the technique, see [57].

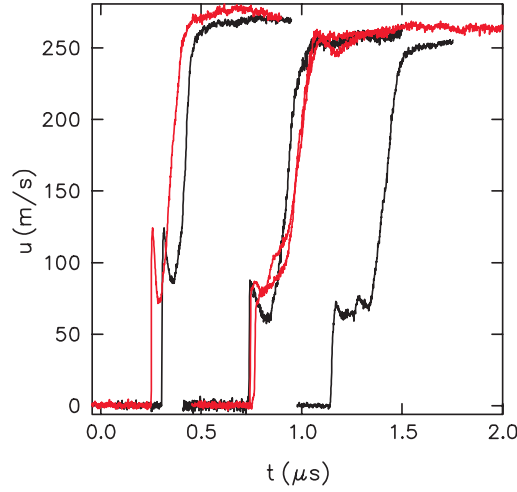


Figure 3. Wave profiles at 1.4 GPa stress in single-crystal HMX. VISAR data from [55, p 27 and figure 34; 56]. Red and black lines are waves normal to the [110] and [011] planes, respectively. The sample length varies from 1.2 to 4.7 mm.

The wave profiles suggest that a viscoplastic model can be used to describe HMX. The simplest model of this type is due to Hohenemser and Prager [59] (see e.g. [60, p 105]). The stress deviator is allowed to overshoot the yield surface and then relax back towards it. The model can be expressed in terms of a differential equation for the stress deviator. In the simple case of an isotropic material,

$$\frac{d}{dt} \sigma' + \frac{G}{\eta} \left(1 - \frac{\sqrt{2/3} Y}{\|\sigma'\|} \right)_+ \sigma' = 2G \frac{d}{dt} \epsilon', \quad (9)$$

where σ and ϵ are the stress and strain tensors, respectively, the prime denotes the deviatoric component of a tensor, Y is the von Mises yield stress, f_+ denotes the positive part of the variable f , i.e. $f_+ = \max(f, 0)$, G is the shear modulus and η is a parameter with dimensions of viscosity.

The experiment with the longest distance of run, shot 1168 [56], can be considered to give the asymptotic wave profile. The model parameters have been adjusted to fit this experiment: $Y = 0.26$ GPa, $G = 12$ GPa and $\eta = 0.11$ GPa μs (1100 Poise⁸). A comparison between the simulation and the data is shown in figure 4. A single profile can be very well fit by the model. However, the model is too simple to describe accurately the transient response. In particular, the model does not reproduce the decrease in velocity immediately behind the elastic precursor for short distances of run. A consequence of not fitting the transient is that the fit significantly overestimates the value of G .

A few comments are in order:

(a) The experiments correspond to uniaxial strain and can be described by the fluid dynamics equations. However, isotropic material properties applied to an anisotropic crystal lead to slight inconsistencies. In the example above, the longitudinal sound speed for the model is $c_1 = [(K + \frac{4}{3}G)/\rho]^{1/2} = 3.96$ mm μs^{-1} while the measured value is 10% lower, 3.72 mm μs^{-1} [55, table 2]. The next section describes the anisotropic response in more detail.

⁸ Poise is the cgs unit of 'dynamic' viscosity and corresponds to 10^{-1} Pa s.

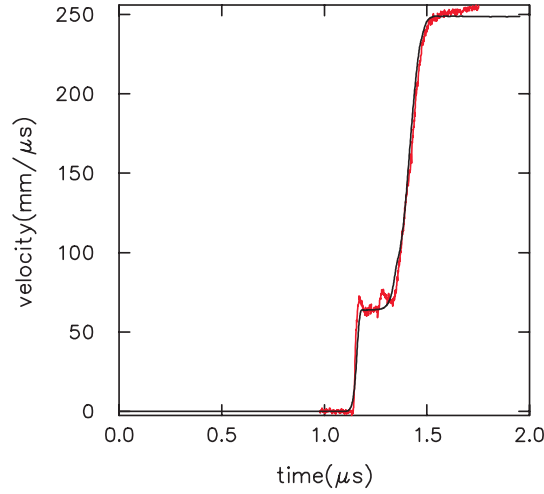


Figure 4. Comparison of wave profile data and the viscoplastic model. The red line is data from shot 1168 [56]: wave normal to the [011] plane after 4.66 mm run distance. The black line is the result of simulation with the viscoplastic model.

(b) Hot-spot temperature in some models based on void collapse is dominated by viscous heating. (Viscous heating is important when the Reynolds number, $\rho u R / \eta$ based on void radius R , is of the order of 1 or less. When the Reynolds number is large, jetting of the void surface may be the source of hot spots.) Typically, the viscous coefficient is a fitting parameter and is chosen in the range of 100–1000 Poise. The viscous coefficient associated with solids is several orders of magnitude greater than for a liquid, which typically is in the range of 0.01–1 Poise. Consequently, melting has a large effect on viscous heating. Moreover, the latent heat significantly decreases the final temperature. In addition, melting affects the dynamics of void collapse, in particular the symmetry of the void and hence the maximum compression⁹.

(c) The reason the viscous coefficients are so different in solids and liquids is due to the different underlying physical mechanisms for viscosity. For a fluid or a gas, viscosity results from diffusion of atoms or molecules, whereas for a solid, viscosity is an approximation to rate-dependent plasticity. The time constant for the relaxation of the stress deviator in equation (9) is $\tau = \eta / G$. In the plastic flow regime, when the strain varies slowly on the time scale of τ , the rate-dependent plastic model is well approximated by a rate-independent elastic–plastic model plus an additional viscous stress with shear viscosity coefficient $\frac{3}{4}\eta = 824$ Poise. We note that this value is compatible with the values used in hot-spot models in which dissipation is dominated by viscosity. Though shear viscosity can be used to fit the rise time of a plastic wave, it would also smear out the elastic precursor. Thus, for split waves there is clear distinction between a viscous model and a rate-dependent plastic model.

(d) The relaxation time associated with plasticity also is evident in the rise time of a compaction wave in a granular bed of HMX. For coarse grains, the rise time decreases with stress, and for large stress approaches the time for the wave to traverse a single grain. If the grain size sets the scale for the rise time, then the rise time would decrease when the bed is composed of finer grains. Experimentally, however, the rise time of a compaction wave approaches 100 ns independent of grain size [61, figure 2.10]. This is comparable with the

⁹ Private communications, Paul Conley, 2000.

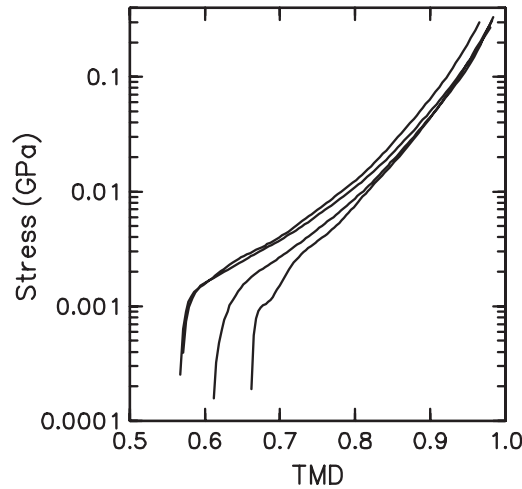


Figure 5. Quasi-static compaction of granular HMX. Data are from Elban and Chiarito [62]. Porosity is approximately $1 - TMD$, where TMD stands for theoretical maximum density but is actually the ratio of granular density to crystal density.

rise time of the plastic wave in the single-crystal experiments, and suggests that the rise time of strong waves is ultimately limited by the plastic response of a crystal rather than the size of a grain.

The yield strength is a key parameter for plasticity. The amplitude of the elastic precursor leads to a value of 0.26 GPa. This is compatible with quasi-static compression experiments [62]. Quasi-static experiments measure porosity as a function of stress for a granular bed. The data for HMX are shown in figure 5. The crush-up stress at which the porosity vanishes is about 0.3 GPa. It is of the order of the yield strength and is about the same as the value obtained from the single-crystal wave profile experiment (0.26 GPa). The crush-up stress is also compatible with experience from manufacturing HMX-based PBXs. Namely, porosity is not completely eliminated at the maximum pressing stress of 20 000 psi (0.135 GPa).

The yield strength can also be estimated from hardness measurements; see e.g. [63]. The experiments of Palmer and Field [64] imply a yield strength of 0.13 GPa, which is about half the value obtained from the experiment discussed above. A possible explanation is that plastic flow occurs when the resolved shear stress reaches a critical value along particular crystallographic slip directions. The strain in the wave profile experiments is approximately uniaxial. The propagation direction may be such that the direction of maximum shear is not aligned with the slip direction. The misalignment would result in the precursor stress having a larger value than the critical shear stress. The indenter used to measure hardness results in a much different strain field, and the yield stress inferred from the hardness measurements may be closer to the critical shear stress.

Gas gun experiments of compaction waves in a granular bed [61] give indirect information on the yield strength. The wave speed depends on the porosity behind the wave front. The porosity in turn depends on plastic deformation, which in turn depends on the yield strength. Simulations [3] with a yield strength of 0.1 GPa agree with the experimental wave speed, whereas with a yield strength of 0.3 GPa the simulated wave speed is substantially larger than the experimental value.

Plastic work is proportional to the product of the yield strength and the equivalent plastic strain. The temperature rise from plastic work is given by $\Delta T = Y\epsilon/\rho C_V$. Deformation of

grains may lead to localized plastic strains of $\epsilon \lesssim 1$. Even with an overestimate of the yield strength, say $Y = 0.3$ GPa, and a low value for specific heat, $C_V = 1 \times 10^{-3}$ MJ kg⁻¹ K⁻¹, the temperature rise from plastic deformation is only moderate, $\Delta T = 150$ K. This implies that either very large shear displacements from grains sliding past each other (in effect, frictional heating) or another mechanism, such as the collapse of voids, is needed to obtain hot spots with sufficiently high temperature in order to achieve a large enough reaction rate for a non-negligible amount of burn to occur before the hot spots quench. Post-test micrographs of PBX samples from shear-impact experiments [65] do show evidence of large shear displacements and cracks within explosive crystals.

4.3. Elastic tensor

Engineering-scale simulations of explosives use a cell size much larger than a grain. Since the grain orientation is random¹⁰, it is reasonable to assume that the average mechanical response of the bulk explosive is isotropic. For an isotropic elastic material, the stress–strain relation is determined by a bulk modulus K and a shear modulus G :

$$\sigma = K(\text{Tr } \epsilon)\mathbb{I} + 2G\epsilon'.$$

There are three acoustic waves: one longitudinal and two transverse. The longitudinal wave speed is $c_l = [(K + \frac{4}{3}G)\rho]^{1/2}$, and both transverse wave speeds are $c_t = (G/\rho)^{1/2}$. Moreover, the wave speeds are independent of the direction of propagation.

However, on the mesoscale needed for simulating hot-spot initiation, the explosive grains are crystalline and hence anisotropic. The stress is related to the strain by the rank 4 elastic tensor

$$\sigma = C : \epsilon.$$

The wave speeds are determined by the eigenvalue equation (see e.g. [66, section 23])

$$\det(n_i C_{ijkl} n_l - \rho c^2 \delta_{j,k}) = 0,$$

where \hat{n} is the direction of propagation. In general, the three wave speeds are distinct and depend on the direction of propagation.

Recently, Zaug [67] has measured the wave speeds for β -HMX as a function of direction in the (0,1,0) plane. The wave speeds were then used to determine the elastic tensor. In addition, molecular dynamics simulations have been used to determine the isothermal elastic tensor directly [9]. The wave speeds determined from both elastic tensors are shown in figure 6. The anisotropy in the quasi-longitudinal sound speed is about $\pm 10\%$. This implies a $\pm 20\%$ variation in the modulus. The effect on the quasi-transverse speeds is larger. In addition, Zaug has measured the sound speeds at an elevated temperature. In contrast to a gas or fluid, the longitudinal sound speed decreases with increasing temperature. Most likely, this effect is due to the decrease in density resulting from thermal expansion¹¹.

Previously, we noted that the δ -phase has a higher reaction rate and is produced when HMX is damaged. Molecular dynamics has been applied to compute the elastic tensor for δ -HMX [13]. The Voigt average bulk modulus is predicted to be 16% higher for the δ -phase than for the β -phase. Consequently, damage resulting in the δ -phase changes the mechanical properties of HMX as well as the sensitivity.

¹⁰ Some manufacturing processes for PBXs, such as ram pressing, may cause the explosive grains to have a preferred direction. This is similar to what is called ‘texture’ that occurs from rolling metal sheets or drawing wire. In such cases, the average stress–strain response of the material would not be isotropic.

¹¹ Recall, from the hydrostatic equation of state, on an isentrope $K' = dK/dP = 4s - 1$ implies that to leading order near the initial state $\rho c^2 = K = K_0(\rho/\rho_0)^{4s-1}$ (where s is the slope of the (shock velocity)–(particle velocity) relation). Since $s > 1$, the sound speed increases with density.

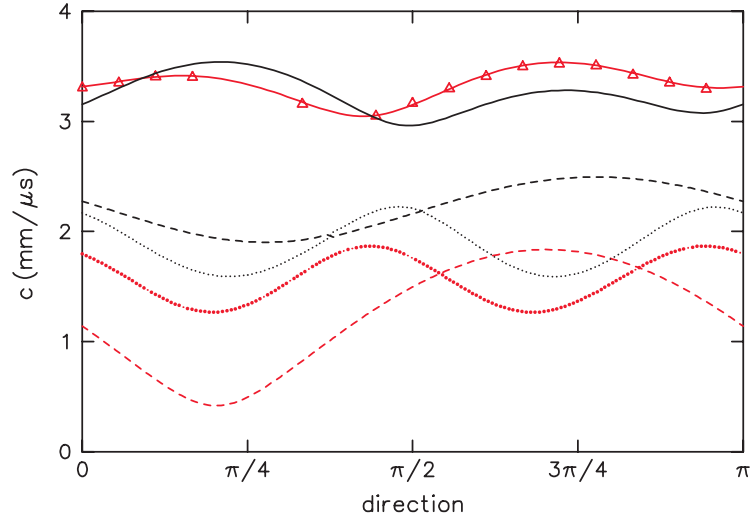


Figure 6. Acoustic wave speed for β -HMX as a function of angle in the (0,1,0) plane at ambient conditions. The red lines are based on the elastic tensor fit to experimental data [67]. The black lines are based on the elastic tensor from molecular dynamics [9]. The solid, dotted and dashed lines correspond to longitudinal, horizontally polarized transverse and vertically polarized transverse waves, respectively. The symbols correspond to the data.

Comparison with experimental data allows the accuracy of the molecular dynamics to be assessed. This is an important step in order to have confidence in molecular dynamics predictions in cases where data are unavailable, such as isotherms for δ -HMX or the liquid phase. It is seen from figure 6 that there is reasonable agreement for the quasi-longitudinal wave speed but not for the quasi-transverse wave speeds. Several comments are in order:

(a) Measurements of the sound speed have been made in only one crystallographic plane. The transverse speeds were only determined for a few directions and were not used in fitting the elastic coefficients. Consequently, there is a large uncertainty in some components of the measured elastic tensor. The transverse velocities plotted in figure 6 are based on the elastic tensor and do not represent measured values. The accuracy of the experimentally determined elastic tensor should improve with sound speed measurements in additional planes.

(b) Zaug's fit of the elastic tensor to the experimental data [67] is constrained to have a Voigt average bulk modulus of 12.5 GPa. This is the value of the isothermal bulk modulus reported by Yoo and Cynn [23]. However, our best least-squares fit to their data resulted in $K_{T_0} = 14.7$ GPa [45]. Furthermore, the acoustic sound speed is related to the isentropic bulk modulus, which is 5.2% larger than the isothermal bulk modulus. Consequently, the fit constrains the average modulus to a value that is 11% low. An additional data point is Dick's measurement of the longitudinal sound speed in the (1,1,0) direction of $3.72 \text{ mm } \mu\text{s}^{-1}$ [55, table 2]. This is 9.8% higher than the value of $3.35 \text{ mm } \mu\text{s}^{-1}$ obtained from the elastic tensor determined by Zaug and well outside the estimated experimental accuracy of 3%. We note that the uncertainty in the elastic tensor from sound speed measurements in a single plane affects the longitudinal Voigt average modulus as well as the transverse sound speeds. Thus, the discrepancy in the acoustic sound speed is very likely due to the constraint placed on the fit to the elastic tensor.

(c) Molecular dynamics calculates the isothermal elastic tensor while the experiment determines the isentropic elastic tensor.

Clearly, these discrepancies need to be corrected in order to make a clean comparison between experiments and molecular dynamics.

The elastic tensor is only part of the anisotropy. The yield surface can also be expected to be anisotropic. Dissipation is due to plastic strain and the plastic strain can be significantly larger than the elastic strain. In addition, when a shock wave transverses a grain, a small void may be a nucleation site for a shear layer¹². Very likely the extent and magnitude of the shear layer depends on the anisotropy of the elastic tensor and the yield surface. Potentially this is a significant hot-spot mechanism. Consequently, the anisotropy of the yield surface is an important question. Again it would be worthwhile to measure the yield surface for sugar, the mechanical mock-up for HMX, and avoid difficulties associated with working with a reactive material.

Anisotropy significantly complicates the flow dynamics. For example, consider the wave profile experiment discussed in the previous section. Though the experiment is designed to achieve uniaxial strain, the non-alignment between stress and strain causes additional weak quasi-transverse waves to be generated. The transverse waves have a slower wave speed than the plastic wave. They are usually ignored since it is not possible to distinguish them by measuring only the longitudinal component of the velocity¹³. Furthermore, for a monoclinic crystal, it follows from the spectral decomposition of the elastic tensor [69, section 8] that the stress cannot be decomposed as in (4) with the hydrostatic component depending only on the density and a deviatoric stress depending only on the strain deviator. In addition, for large shear strain there are questions on how to model the rotational part of the plastic strain rate tensor. In view of these complications, it would be worthwhile to consider whether the main effects of anisotropy could be simulated with added heterogeneities on the mesoscale, namely, each grain modelled as having an isotropic response but with moduli and yield strength randomly assigned from distributions chosen to mock-up the true crystal anisotropy.

5. Transport properties

5.1. Heat conduction

Thermal conductivity, as a function of temperature at atmospheric pressure, has been measured for β -HMX [43, 44] and computed from molecular dynamics for the liquid phase [8]. The measured values of the two experiments show the same trend, but the values at a given temperature differ by 50%. Here we use values from the later experiment [44] which has the higher values for conductivity. In the solid phase, the conductivity decreases linearly with temperature. At melting it has a value of $\lambda = 3.6 \times 10^{-3} \text{ J cm}^{-1} \text{ s}^{-1} \text{ K}^{-1}$. The conductivity continues to decrease in the liquid phase with roughly the same slope until about 700 K, where it levels off with a value of $\lambda \approx 2.6 \times 10^{-3} \text{ J cm}^{-1} \text{ s}^{-1} \text{ K}^{-1}$.

The thermal diffusivity is given by

$$k = \frac{\lambda}{\rho C_P}.$$

At melting, $k = 0.13 \text{ mm}^2 \text{ s}^{-1} = 0.13 \mu\text{m}^2 \mu\text{s}^{-1}$. On the microsecond scale of the induction time for a hot spot, heat conduction affects only very small distances, $\Delta x \approx \sqrt{k \Delta t} = 0.36 \mu\text{m}$. In contrast, on the hour time scale of a cook-off experiment, the length scale associated with heat conduction is of the order of centimetres.

¹² Private communications, Paul Conley, 2000.

¹³ There are experimental techniques for measuring both the longitudinal and transverse components of the strain tensor, see e.g. [68]. However, these techniques are not well developed and have not been applied to explosives.

Heat conduction is a critical factor in a deflagration wave. An upper bound on the wave speed can be estimated as follows. Heat flow from the front raises a layer Δx of reactants to the ignition temperature which then burns in a time Δt . The wave speed is $D = \Delta x / \Delta t$. If the heat flow is due to conduction, then $\Delta x = \sqrt{k \Delta t}$ and $D = \sqrt{k / \Delta t}$. The reaction time of a detonation wave provides a lower bound for Δt . For HMX-based PBX-9501 the measured detonation velocity is $8.8 \text{ mm } \mu\text{s}^{-1}$ and the reaction zone width is a few 0.1 mm , resulting in $\Delta t \gtrsim 0.01 \text{ } \mu\text{s}$; see [2, table 1.4, p 23; 70]. With this reaction time, the width of the flame front is $\Delta x = 0.036 \text{ } \mu\text{m}$ (about 36 molecules wide) and gives, as an upper bound for the deflagration wave speed, $D < 3.6 \text{ m s}^{-1}$. At this speed, an explosive pellet of thickness 0.1 mm would take $15 \text{ } \mu\text{s}$ to burn completely, which is long compared to $0.01 \text{ } \mu\text{s}$ time for a detonation wave to transit a grain. We note that shock desensitization experiments imply that hot spots from void collapse are necessary to propagate a detonation wave. Consequently, heat conduction is not the mechanism for the growth of hot spots.

Experiments show that the deflagration wave speed depends on pressure. For HMX, when pressure is increased starting at 1 atm , the wave speed increases from a few mm s^{-1} to a few cm s^{-1} . At a critical pressure, which depends on porosity (about 100 bar for 5% porosity), the wave speed jumps to a few tens of m s^{-1} [71]. Fast deflagrations are associated with convective burning, i.e. heat flow is dominated by convection of hot reaction product gases through the pores rather than conduction. Permeation over a distance of one or two grains would be sufficient to raise the next grain to the ignition temperature. The wave speed is compatible with a particle velocity estimated from $\Delta u = \Delta P / \rho c$. Verifying convective burn and predicting the critical pressure are problems well suited to mesomechanics simulations. Since packing of grains and the connectivity of pores depend on the spatial dimension, simulations would have to be performed in three dimensions.

5.2. Viscosity

For the liquid phase of HMX, the shear viscosity has been determined from molecular dynamics simulations [7]. The value of the viscosity coefficient is $\eta = 4.5 \text{ Poise}$ at melting (550 K) and decreases with temperature following an Arrhenius law, $\eta = \eta_0 \exp(T_a / T)$, with an activation temperature of $T_a = 7800 \text{ K}$ and $\eta_0 = 3.1 \times 10^{-6} \text{ Poise}$. At 800 K the viscosity coefficient drops to $\eta = 0.055 \text{ Poise}$.

The viscosity coefficient for the liquid phase is orders of magnitude smaller than that of the solid phase. For comparison, the single-crystal plastic wave profile discussed in section 4.2 is fit with a viscosity coefficient of $\eta \sim 1000 \text{ Poise}$. Consequently, viscous heating after melting is a small effect unless the shear strain is large.

Large shear strains can only occur in thin layers. Simple estimates of viscous heating are instructive. Consider a shear layer with a jump in tangential velocity $\Delta u \sim u$ and a thickness Δx . The viscous stress is given by $Q = \eta(\Delta u / \Delta x)$. The temperature rise after a time Δt is given by

$$\begin{aligned} \Delta T &= \frac{Q u A \Delta t}{C_P \rho A \Delta x} \\ &= \frac{\eta u^2 \Delta t}{C_P \rho (\Delta x)^2}. \end{aligned}$$

We note that A , the area of the shear layer, drops out. The temperature rise is maximum when Δx has the minimum value allowed by heat conduction, $(\Delta x)^2 / \Delta t \sim k$. Hence,

$$\Delta T_{\max} = \frac{\eta u^2}{\lambda}. \quad (10)$$

Assuming $u \sim 0.1 \text{ mm } \mu\text{s}^{-1}$ and with parameter values at the melting temperature, $\Delta T_{\text{max}} = 1.2 \times 10^4 \text{ K}$. The decrease in viscosity with temperature greatly reduces the temperature rise. Thermal softening also serves to keep the shear layer narrow. Evaluating (10) with the values of viscosity and thermal conductivity at 800 K reduces the maximum temperature rise to 210 K. Since viscosity decreases rapidly with temperature, the hot-spot temperature induced by a shear layer is probably limited to 900 K at atmospheric pressure.

Viscosity increases with pressure and this would partly offset the decrease with temperature from shear heating. Bridgman [72] and Frey [73] have used the fitting form

$$\eta(T, P) = \eta_0 \exp\left(\frac{P}{P_0}\right) \exp\left(\frac{T_0}{T}\right). \quad (11)$$

Conley [74, pp 122–6] proposed a modified form

$$\eta(T, P) = \eta_0 \exp\left(\frac{T_0 P}{T P_0}\right), \quad (12)$$

and for HMX used $P_0 = 0.165 \text{ GPa}$. Since a confining pressure would increase the temperature rise of a shear layer, and hence the decomposition rate within the layer, it would be worthwhile extending the molecular dynamics calculations to determine the full pressure and temperature dependence of viscosity.

We note that on a time scale of $\Delta t = 1 \mu\text{s}$, the diffusion length is $\Delta x \sim \frac{1}{3} \mu\text{m}$ and the viscous stress Q ranges from 0.14 GPa at 550 K to 0.0016 GPa at 800 K. The shear strain is indeed very large, $\epsilon = u \Delta t / \Delta x = 300$. The relative slip $u \Delta t = 0.1 \text{ mm}$ is on the order of a grain diameter. The shear layer is very narrow, about 300 molecules wide. This is likely to occur in the melt layer between grains sliding past each other or along closed cracks, as advocated by Dienes [75] as the dominant dissipative mechanism for generating hot spots and incorporated in his SCRAM model.

The rapid heating of a shear layer will cause it to burn on a submicrosecond time scale. Rapid burning greatly increases the pressure within a shear layer. The subsequent expansion will quench the reaction. Consequently, to release a significant amount of energy the cumulative area of shear layers needs to be large. In general, a single hot spot has a small volume and is not sufficient to initiate a detonation wave. Mesomechanical simulations of explosives can be used to determine how hot spots are generated, and then follow the evolution of hot spots in order to understand the collective effects responsible for the initiation of a detonation wave.

6. Open questions

Experiments show that lightly confined HMX-based PBX-9501 when impacted by blunt projectiles at relatively low velocities, $50\text{--}100 \text{ m s}^{-1}$, undergoes violent delayed reaction [32]. Recovered samples of explosive from impacts below the threshold velocity for violent reaction show evidence of cracking and surface melt layers.

These experiments indicate that in order to understand hot-spot initiation for such weak stimuli, two additional mechanical properties are of major importance: fracture and crystal defects. These issues are briefly discussed.

6.1. Cracks

Wiegand [76] has measured the stress–strain response of PBS-9501 (plastic-bonded sugar mock-up for PBX-9501). His data are reproduced in figure 7. They show that there is a qualitative difference in the response of a confined and unconfined material.

Without confinement, above a threshold stress the material displays dilatancy, i.e. a decrease in strain with increasing stress. This response is associated with the nucleation

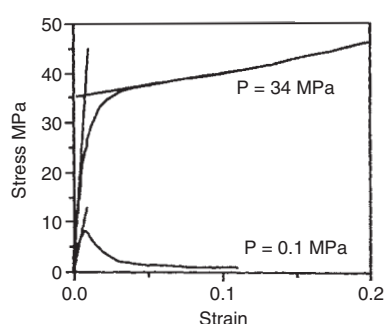


Figure 7. Stress–strain relation for confined and unconfined PBS-9501. Reproduced from Wiegand [76, figure 1] (with permission of the author). The values of P correspond to the confinement pressure.

and growth of cracks in a brittle material. In contrast, with a small confining stress of 340 bar, the response is typical of a ductile material, i.e. elastic–plastic with work hardening.

Dilatancy implies that the slope of the stress–strain curve changes sign. Since the slope is proportional to the square of the sound speed, a negative slope implies non-equilibrium behaviour. Accounting for the effect of cracks requires additional internal degrees of freedom, such as porosity, and associated governing equations.

Visco-SCRAM¹⁴ [77] is an example of one such model. It is a homogenized isotropic model representing a coarse grain average and is suitable for engineering simulations. However, it is not appropriate at the grain scale. Models that account for fracture and growth of cracks in explosive crystals are needed for mesoscale simulations of unconfined or weakly confined PBXs.

6.2. Defects

Explosive grains used in a PBX are not perfect crystals. The defects depend on the manufacturing process. A study of an RDX-based PBX found that there is a large variation in ignition sensitivity as measured by the Pop plot (distance of run to detonation as a function of pressure) [78]. The experiments held the density fixed and therefore demonstrate that in addition to porosity other factors can significantly affect sensitivity.

Previously, the size distribution of HMX grains used in PBXs had been measured. More recent efforts are aimed at characterizing the microstructure; see e.g. [65, 16]. In addition, the process of pressing moulding powder into a PBX introduces cracks and twinning defects in HMX grains [17]. Understanding which defects or aspects of the microstructure dominate initiation sensitivity is an important problem because it determines what effects must be incorporated into mesoscale simulations.

At least three fairly well characterized PBXs are based on HMX: PBX-9501, LX-10 and EDC-37. One goal of mesoscale simulations should be to understand the relative ignition sensitivity of these explosives. This is a necessary validation step for predicting the effects of ageing.

7. Summary

Physics-based simulations of initiation in a PBX require resolving explosive grains. Hence, a detailed knowledge of the constitutive properties of explosive crystals is needed. Simulations to

¹⁴ Visco-SCRAM is a simplified version of John Dienes' Statistical Crack Mechanics.

date (e.g. [3–5]) have used crude material models for HMX. The most important shortcomings are in the hydrostatic equation of state and the simplification of a constant specific heat. As discussed in section 4.1, the Mie–Grüneisen equation of state currently used is significantly different from the more recent Birch–Murnaghan form. Taking all the data into account, we think the Birch–Murnaghan form more accurately represents HMX. As discussed in section 3.2, the temperature dependence of the specific heat has a significant effect on hot-spot temperature. It must be taken into account in order to calculate reaction rates.

The dissipative mechanism generating hot spots depends on the strength and type of stimulus the explosive is subjected to. In the weak regime (pressure of the order of or less than the yield strength), the hot-spot temperature in simulations to date [3, 4] is below the melting temperature. This is not consistent with gas gun experiments which show that some reaction takes place on the μs time scale of the experiment. Those simulations assume plastic work is the dominant dissipative mechanism. The low temperature in the simulations is compatible with our estimates in section 4.2 of the plastic work. Very likely the dominant dissipative mechanism in this regime is frictional work at the interface between grains. Mesoscale simulations are currently performed with Eulerian algorithms. A property of Eulerian algorithms is that velocity shear is not well represented at material interfaces. This case illustrates that it is not enough to input parameters such as shear viscosity, but the numerical algorithm must also be capable of accurately representing the physics. We have given estimates of the resolution associated with viscosity and heat conduction in sections 5.2 and 5.1, respectively.

In the regime of shock-to-detonation transitions in a PBX, the dominant dissipative mechanism is undoubtedly microjetting when a void implodes. In order to resolve grains and interstitial pores within a PBX, three-dimensional simulations on current supercomputers [5] are limited to a physical domain $\sim (1\text{ mm})^3$ and a run time $\sim 1\text{ }\mu\text{s}$. To see a build-up to detonation on these spatial and temporal scales, it would be necessary to start with a strong shock. Based on the Pop plot for PBX-9404 (which is a sensitive HMX-based explosive) [2, figure 4.2, p 192], an initial shock pressure in excess of 150 kb is required. To gain more intuition on hot-spot initiation from numerical simulations, simplified model problems are needed.

Finally, we note that several properties of HMX are not adequately known. The most critical of these are: (i) the melt curve as a function of pressure; (ii) the specific heat in the liquid phase as a function of T ; (iii) the viscosity in the liquid phase as a function of P and T ; (iv) the anisotropy in the yield surface. It is difficult to measure experimentally quantities in the liquid phase because of the rapid onset of decomposition. Yet on the microsecond or millisecond time scale of initiation events, the non-equilibrium phases must be considered. Molecular dynamics simulations are a means of determining the values of some of the parameters for the thermodynamic regions of interest. The accuracy of molecular dynamics can only be assessed by comparing with data where available.

Although it has not been the focus of this paper, chemical reaction rates are obviously required for studying hot-spot initiation. While reaction rates depend sensitively on temperature, to explain the insensitivity of a single crystal and shock desensitization of heterogeneous explosives, the pressure dependence of the reaction rate also should be determined.

Acknowledgments

The authors thank Jerry Dick for sharing his data and discussions on properties of HMX, Joe Zaig for sharing his data on the elastic constants of HMX, and Grant Smith and Dmitry Bedrov for close collaboration in published and ongoing molecular dynamics simulations of HMX.

References

- [1] Bowden F P and Yoffe Y D 1952 *Initiation and Growth of Explosion in Liquids and Solids* (Cambridge: Cambridge University Press)
- [2] Mader C L 1998 *Numerical Modeling of Explosives and Propellants*. 2nd edn (Boca Raton, FL: CRC Press)
- [3] Menikoff R 2001 Compaction wave profiles: gas gun experiments and simulations *J. Appl. Phys.* **90** 1754–60
- [4] Baer M R and Trott W M 2001 Mesoscale descriptions of shock-loaded heterogeneous porous materials *Shock Compression of Condensed Matter 2001* (New York: AIP)
- [5] Baer M R 2002 Modeling heterogeneous energetic materials at the mesoscale *Thermochim. Acta* at press
- [6] Leiber C-O 2000 Aspects of the mesoscale of crystalline explosives *Propellants, Explosives, Pyrotechnics* **25** 288–301
- [7] Bedrov D, Smith G D and Sewell T D 2000 Temperature dependent shear viscosity coefficients of HMX, a molecular dynamics simulation study *J. Chem. Phys.* **112** 7203–8
- [8] Bedrov D, Smith G D and Sewell T D 2000 The thermal conductivity of liquid HMX from molecular dynamics simulations *Chem. Phys. Lett.* **324** 64–8
- [9] Ayyagari C, Bedrov D, Smith G D, Sewell T D, Menikoff R and Zaug J M 2001 Molecular dynamics simulations of HMX crystal polymorphs using a flexible molecule force field *J. Comput. Aided Mater. Design* at press, LA-UR-00-2377, <http://t14web.lanl.gov/Staff/tds/preprints.html#HMX-validate>
- [10] Sewell T D 1998 Monte Carlo calculations of the hydrostatic compression of hexahydro-1,3,5-trinitro-1,3,5-triazine and beta-octahydro-1,3,5,7-tetranitro-1,3,5,7-tetrazocine *J. Appl. Phys.* **83** 4142–5
- [11] Sorescu D C, Rice B M and Thompson D L 1998 Isothermal–isobaric molecular dynamics simulations of 1,3,5,7-tetranitro-1,3,5,7-tetraazacyclooctane (HMX) crystals *J. Phys. Chem. B* **102** 6692–5
- [12] Sorescu D C, Rice B M and Thompson D L 1999 Theoretical studies of the hydrostatic compression of RDX, HMX, HNIW, and PETN crystals *J. Phys. Chem. B* **103** 6783–90
- [13] Sewell T D, Bedrov D, Menikoff R and Smith G D 2001 Elastic properties of HMX *Shock Compression of Condensed Matter 2001* (New York: AIP)
- [14] Bedrov D, Smith G D and Sewell T D 2001 Molecular dynamics simulations of HMX crystal polymorphs using a flexible molecule force field *Shock Compression of Condensed Matter 2001* (New York: AIP)
- [15] Henson B F, Asay B W, Smilowitz L B and Dickson P M 2001 Ignition chemistry in HMX from thermal explosion to detonation *Technical Report LA-UR-01-3499*, Los Alamos National Laboratory, <http://lib-www.lanl.gov/la-pubs/00818477.pdf>
- [16] Skidmore C B, Phillips D S, Idar D J and Son S F 1999 Characterizing the microstructure of selected high explosives *Technical Report LA-UR-99-1201*, Los Alamos National Laboratory, <http://lib-www.lanl.gov/la-pubs/00357085.pdf>
- [17] Skidmore C B, Phillips D S, Howe P M, Mang J T and Romero J A 1998 The evolution of microstructural changes in pressed HMX explosives *Proc. 11th Detonation Symp.* pp 556–64
- [18] Cady H H and Smith L C 1962 Studies on the polymorphs of HMX *Technical Report LAMS-2652*, Los Alamos Scientific Laboratory, <http://lib-www.lanl.gov/la-pubs/00371090.pdf>
- [19] Cady H H, Larson A C and Cromer D T 1963 The crystal structure of α -HMX and a refinement of the structure of β -HMX *Acta Crystallogr.* **16** 617–23
- [20] Choi C S and Boutin H P 1970 A study of the crystal structure of β -cyclotetramethylene tetranitramine by neutron diffraction *Acta Crystallogr. B* **26** 1235–40
- [21] Cobbleddick R E and Small R W H 1974 The crystal structure of the δ -form of 1,3,5,7-tetranitro-1,3,5,7-tetraazacyclooctane (δ -HMX) *Acta Crystallogr. B* **30** 1918–22
- [22] Main P, Cobbleddick R E and Small R W H 1985 Structure of the 4th form of 1,3,5,7-tetranitro-1,3,5,7-tetraazacyclooctane (γ -HMX) *Acta Crystallogr. C* **41** 1351–4
- [23] Yoo C-S and Cynn H 1999 Equation of state, phase transition, decomposition of β -HMX *J. Chem. Phys.* **111** 10229–35
- [24] Herrmann M, Engel W and Eisenreich N 1993 Thermal analysis of the phases of HMX using x-ray diffraction *Z. Kristallogr.* **204** 121–8
- [25] Karpowicz R J and Brill T B 1982 Solid phase transition kinetics: the role of intermolecular forces in the condensed-phase decomposition of octahydro-1,3,5,7-tetranitro-1,3,5,7-tetrazocine *J. Phys. Chem.* **86** 4260–5
- [26] Henson B F, Asay B W, Sanders R K, Son S F, Robinson J M and Dickson P M 1999 Dynamic measurements of the HMX β – δ phase transition by second harmonic generation *Phys. Rev. Lett.* **82** 1213–6
- [27] Herrmann M, Engel W and Eisenreich N 1992 Thermal expansion, transitions, sensitivities and burning rates of HMX *Propellants, Explosives, Pyrotechnics* **17** 190–5

- [28] Dickson P M, Asay B W, Henson B F, Fugard C S and Wong J 1999 Measurements of phase change and thermal decomposition kinetics during cookoff of PBX-9501 *Shock Compression of Condensed Matter* pp 837–40
- [29] Hall P G 1971 Thermal decomposition and phase transitions in solid nitramines *Trans. Faraday Soc.* **67** 556–62
- [30] Karpowicz R J and Brill T B 1982 The $\beta \rightarrow \delta$ transition of HMX: its thermal analysis and relationship to propellants *AIAA J.* **20** 1586–91
- [31] Howe P M, Dickson P M, Henson B F, Asay B W, Smilowitz L B, Greenfield M T, Bennett J G and Gerken J M 2000 Thermal response of explosives systems *Technical Report* LA-UR-00-2959, Los Alamos National Laboratory, <http://lib-www.lanl.gov/la-pubs/00393590.pdf>
- [32] Idar D J, Straight J W, Osborn M A, Skidmore C B, Phillips D S and Buntain G A 2000 PBX-9501 high explosive violent reaction: phase II baseline and aged experiment *Technical Report* LA-13641-MS, Los Alamos National Laboratory, <http://lib-www.lanl.gov/la-pubs/00538217.pdf>
- [33] Poirier J-P 1991 *Introduction to the Physics of the Earth's Interior* (Cambridge: Cambridge University Press)
- [34] Olinger B, Roof B and Cady H H 1978 The linear and volume compression of β -HMX and RDX *Proc. Int. Symp. on High Dynamic Pressures* (Paris: CEA) pp 3–8
- [35] Massoni H and Saurel R 1999 A mechanistic model for shock initiation of solid explosives *Phys. Fluids* **11** 710–36
- [36] Koshigoe L G, Shoemaker R L and Taylor R E 1984 Specific heat of HMX *AIAA J.* **22** 1600–01
- [37] NIST, Chemistry webbook, <http://webbook.nist.gov/chemistry>, Search for HMX
- [38] Sheffield S A, Gustavsen R L and Alcon R R 1997 Porous HMX initiation studies—sugar as an inert simulant *Shock Compression of Condensed Matter* pp 575–8
- [39] Brown G M and Levy H A 1973 Further refinement of the structure of sucrose based on neutron-diffraction data *Acta Crystallogr. B* **29** 790–7
- [40] Hanson J C, Sieker L C and Jensen L H 1973 Sucrose: x-ray refinement and comparison with neutron refinement. *Acta Crystallogr. B* **29** 797–808
- [41] Lyman J L, Liao Yeong-Cherng and Brand H V 2000 Thermochemical functions for gas-phase 1,3,5,7-tetranitro-1,3,5,7-tetraazacyclooctane (HMX), its condensed phases and its larger reaction products *Combust. Flame* accepted, LA-UR-00-2543
- [42] Ward M J, Son S F and Brewster M Q 1998 Steady deflagration of HMX with simple kinetics: a gas phase chain reaction model *Combust. Flame* **114** 556–68
- [43] Shoemaker R L, Stark J A and Taylor R E 1985 Thermophysical properties of propellants *High Temp.–High Pressures* **17** 429–35
- [44] Hanson-Parr D M and Parr T P 1999 Thermal properties measurements of solid rocket propellant oxidizers and binder materials as a function of temperature *J. Energetic Mater.* **17** 1–47
- [45] Menikoff R and Sewell T D 2001 Fitting forms for isothermal data *High Press. Res.* **21** 121–38
- [46] Marsh S ed 1980 *LASL Shock Hugoniot Data* (Berkeley, CA: University of California Press) <http://lib-www.lanl.gov/books/shd.pdf>
- [47] Craig B G 1974 Data from shock initiation experiments *Technical Report* M-3-QR-74-1, Los Alamos Scientific Laboratory
- [48] Olinger B, Halleck P M and Cady H H 1975 The isothermal linear and volume compression of PETN to 10 GPa and the calculated shock compression *J. Chem. Phys.* **62** 4480–3
- [49] Dick J J 1983 A comparison of the shock and static compression curves for four solid explosives *J. Energetic Mater.* **1** 275–86
- [50] Bernecker R R 1985 Observations on the Hugoniot for HMX *Shock Compression of Condensed Matter* pp 141–4
- [51] Hayes D B 1974 Polymorphic phase transformation rates in shock-loaded potassium chloride *J. Appl. Phys.* **45** 1208–16
- [52] Andrews D J 1973 Equation of state of the alpha and epsilon phases of iron *J. Phys. Chem. Solids* **34** 825–40
- [53] Rogers R N 1975 Thermochemistry of explosives *Thermochim. Acta* **11** 131–9
- [54] Lee E L, Sanborn R H and Stromberg H D 1970 Thermal decomposition of high explosives at static pressures 10–50 kilobars *Proc. 5th Detonation Symp.* pp 331–7
- [55] Dick J J, Martinez A R and Hixson R S 1998 Plane impact response of PBX-9501 and its components below 2 GPa *Technical Report* LA-13426-MS, Los Alamos National Laboratory, <http://lib-www.lanl.gov/la-pubs/00418374.pdf>
- [56] Dick J J and Menikoff R 2001 Analysis of wave profiles for single crystal HMX, in preparation, LA-UR-01-574
- [57] Barker L M 1999 The development of the VISAR, and its use in shock compression science *Shock Compression of Condensed Matter* pp 11–17
- [58] Dick J J and Martinez A R 2001 Elastic precursor decay in HMX explosive crystals *Technical Report* LA-UR-01-3338, Los Alamos National Laboratory, <http://lib-www.lanl.gov/la-pubs/00796424.pdf>

- [59] Hohenemser K and Prager W 1932 Beitrag zur mechanik des bildsamen verhaltens von flubstahl *Z. Angew. Math. Mech.* **12** 1–14
- [60] Lubliner J 1990 *Plasticity Theory* (London: Macmillan)
- [61] Sheffield S A, Gustavsen R L and Anderson M U 1997 Shock loading of porous high explosives *High-Pressure Shock Compression of Solids IV: Response of Highly Porous Solids to Shock Compression* ed L Davison, Y Horie and M Shahinpoor (New York: Springer) ch 2 pp 23–61
- [62] Elban W L and Chiarito M A 1986 Quasi-static compaction study of coarse HMX explosive *Powder Technol.* **46** 181–93
- [63] Mohan V K, Bhasu V C J and Field J E 1989 Role of adiabatic shear bands in initiation of explosives by drop-weight impact *9th Int. Symp. on Detonation (Portland, OR, 28 Aug. 1989)* pp 1276–83 OCNR 113291-7, Office of the Chief of Naval Research, Arlington, VA
- [64] Palmer S J P and Field J E 1982 The deformation and fracture of β -HMX *Proc. R. Soc. A* **383** 399–407
- [65] Skidmore C B, Phillips D S, Asay B W, Idar D J, Howe P M and Bolme D S 1999 Microstructural effects in PBX-9501 damaged by shear impact *Shock Compression of Condensed Matter* pp 659–62
- [66] Landau L D and Lifshitz E M 1970 *Theory of Elasticity* (Oxford: Pergamon)
- [67] Zaug J M 1998 Elastic constants of β -HMX and tantalum, equation of state of supercritical fluids and fluid mixtures and thermal transport determinations *Proc. 11th Detonation Symp.* pp 498–509
- [68] Asay J R and Chhabildas L C 1980 Some new developments in shock wave research *High Pressure Science and Technology (Proc. VIIIth Int. AIRAPT Conf.)* ed B Vodar and P Marteau (Oxford: Pergamon)
- [69] Theocaris P S and Sokolis D P 1999 Spectral decomposition of the linear elastic tensor for monoclinic symmetry *Acta Crystallogr. A* **55** 635–47
- [70] Gustavsen R L, Sheffield S A and Alcon R R 1998 Progress in measuring detonation wave profiles in PBX-9501 *Proc. 11th Detonation Symp.* pp 821–7
- [71] Fifer R A and Cole J E 1981 Transition from laminar burning for porous crystalline explosives *Proc. 7th Detonation Symp.* pp 164–74
- [72] Bridgman P W 1949 *The Physics of High Pressure* (London: Bell and Sons)
- [73] Frey R 1981 The initiation of explosive charges by rapid shear *Proc. 7th Detonation Symp.* pp 36–42
- [74] Conley P 1999 Eulerian hydrocode analysis of reactive micromechanics in the shock initiation of heterogeneous energetic material *PhD Thesis* Department of Mechanical Engineering, University of California, San Diego
- [75] Dienes J K 1996 A unified theory of flow, hot spots, and fragmentation with an application to explosive sensitivity *High-Pressure Shock Compression of Solids II: Dynamic Fracture and Fragmentation* ed L Davison, D Grady and M Shahinpoor (New York: Springer) ch 14 pp 366–98
- [76] Wiegand D A 1999 The influence of confinement on the mechanical properties of energetic materials *Shock Compression of Condensed Matter—1999, Proc. American Physical Society Topical Group on Shock Compression of Condensed Matter (Snowbird, UT)* (New York: American Institute of Physics) pp 675–8
- [77] Bennett J G, Haberman K S, Johnson J N, Asay B W and Henson B F 1998 A constitutive model for the non-shock ignition and mechanical response of high explosives *J. Mech. Phys. Solids* **46** 2303–22
- [78] Baillou F, Dartyge J M, Pyckerelle C S and Mala J 1993 Influence of crystal defects on sensitivity of explosives *Proc. 10th Detonation Symp.* pp 816–23